



**HAL**  
open science

# **H induced decohesion of an Al grain boundary investigated with first principles: General conditions for instant breakage and local delayed fracture**

F.J.H. J H Ehlers, M. Seydou, D. Tingaud, F. Maurel, Y. Charles, S. Queyreau

## **► To cite this version:**

F.J.H. J H Ehlers, M. Seydou, D. Tingaud, F. Maurel, Y. Charles, et al.. H induced decohesion of an Al grain boundary investigated with first principles: General conditions for instant breakage and local delayed fracture. Computational Materials Science, 2019, pp.109403. <10.1016/j.commatsci.2019.109403>. <hal-02367144>

**HAL Id: hal-02367144**

**<https://sorbonne-paris-nord.hal.science/hal-02367144v1>**

Submitted on 17 Nov 2019

HAL is a multi-disciplinary open access archive for the deposit and dissemination of scientific research documents, whether they are published or not. The documents may come from teaching and research institutions in France or abroad, or from public or private research centers.

L'archive ouverte pluridisciplinaire HAL, est destinée au dépôt et à la diffusion de documents scientifiques de niveau recherche, publiés ou non, émanant des établissements d'enseignement et de recherche français ou étrangers, des laboratoires publics ou privés.



HAL Authorization

H induced decohesion of an Al grain boundary investigated with first principles:

General conditions for instant breakage and local delayed fracture

F. J. H. Ehlers<sup>1,2</sup>, M. Seydou<sup>1</sup>, D. Tingaud<sup>2</sup>, F. Maurel<sup>1</sup>, Y. Charles<sup>2</sup>, S. Queyreau<sup>2</sup>

<sup>1</sup>University Paris Diderot, Sorbonne Paris Cité, ITODYS, UMR 7086 CNRS, 15 rue J.-A. de Baïf, 75205 Paris cedex 13, France

<sup>2</sup>Université Paris 13, Sorbonne Paris Cité, Laboratoire des Sciences des Procédés et des Matériaux, LSPM, CNRS, UPR 3407, 99 avenue Jean-Baptiste Clément, F-93430 Villetaneuse, France

Abstract

The uniaxial tensile test response of a H decorated  $\Sigma 5$  [100] twist grain boundary (GB) in face-centred-cubic Al has been examined with first principles. The impurity shows a strong tendency to relocate during loading. To capture these H movements, the standard model framework was extended to probe loading-unloading hysteresis. Due to the strong monotonic decrease in the H formation energy with rising GB elongation, the maximum tensile stress accepted by the H decorated GB in the slow fracture limit generally is reached before breakage becomes thermodynamically favourable. For any intact GB configuration visited upon exceeding this stress, the assumption of global chemical equilibrium is argued to be violated. Moreover, while breakage remains ensured from the slow fracture limit considerations, it may in practice require the influx of H to the GB vicinity. A quantitative analysis of GB destabilisation in this scenario requires multi-scale modelling even in the slow fracture limit.

Keywords

Fracture, Grain boundary, H embrittlement, Aluminium, First-principle calculation

## 1. Introduction

Hydrogen induced decohesion (HID) is a prominent, yet controversial [1] member among the candidates for hydrogen embrittlement (HE). When HID is operative, H impurities agglomerate at locations of high hydrostatic stress, drastically reducing the strength of adjacent metal host atom bonds, thus in turn affecting the material toughness and ductility – the trademarks of HE. Atomistic simulations have long supported a detrimental effect of H [2–4]. Experimentally, an increased crack tip sharpness with H concentration has been observed in cleavage studies for some materials (see e.g. [5]), indicating a change from ductile towards brittle behaviour. However, the *relative importance* of HID remains debated, with complications arising from two factors: (i) HE in general incorporates both plastic and elastic contributions, implying that HID is in direct competition with other mechanisms [1, 6, 7]. (ii) Detection of H *in situ* is highly challenging [8]. This fact obstructs an experimental analysis where the impurity influence during a fracture process is quantified with reference to local concentration.

Technically, theoretical studies are not limited in the same manner and hence may provide the missing pieces of the puzzle if applied in conjunction with experiment. If the HE process were clearly dominated by HID, it would seem an acceptable approximation to assume a purely elastic crack tip response. For this situation, *ab initio* modelling applied to the heart of the fracture region may generate accurate results if appropriately coupled structurally and chemically to the surrounding grains. Such modelling would appear particularly intriguing for the case of intergranular fracture, where a satisfactory determination of the H decorated grain boundary (GB) loading response is potentially out of reach for semi-empirical potentials. In the absence of detailed knowledge on the H-GB interactions during loading, large-scale schemes (e.g., using finite element modelling) have so far resorted to treating the GB as a simple 2D surface hosting only one unique trapping site [9].

Several works have analysed the H influence on a decohering metal GB with *ab initio* simulations [4, 10–13], in some cases clearly supporting a destabilising influence of the impurity. In most scenarios examined, however, any H influx from the bulk lattice to the region under investigation has been suppressed, with presently only one work [13] probing this issue via an indirect method. Considering that the H mobility in

these systems is often appreciable, it seems a valid question to ask if important changes to the existing HID picture will be introduced by allowing for an evolving impurity distribution, reflecting stress sensitive H-GB interactions. The present paper focusses on the aspects of this problem relating to the immediate vicinity of the GB plane: through first principles simulations, the influence of both changing H concentration and impurity relocation on the GB sites is examined at a preliminary stage, without explicit requirements for multi-scale modelling. In the same process, the ability of existing zero-temperature formalisms to capture the most reliable state of the GB is addressed. From a more general perspective, the question of possible GB instability modes is revisited: building upon earlier considerations [14], the attempt is made to outline all categories of HID based paths to fracture for the selected type of model system. The link to the evolving H affinity for the GB during loading is discussed, with analytical expressions presented.

As the main focus of this work is to reveal trends in the influence of a changing H distribution on a decohering GB, the optimal choice of test system would seem a GB that hardly binds H at zero load but displays a significant H trapping ability as breakage is approached. The case of face-centred cubic (fcc) Al appears interesting in this context, as potentially supported by experiments [15]. Recently, a highly favourable H site was predicted [16] upon sub-grain displacement in bulk Al. The impurity was located at a ‘bridge (B) type’ site between a metal host pair, with a coordination number of two. For most GBs, such a site should appear upon sufficient loading, as a consequence of sequential bond breakage and increasing alignment of remaining bonds with the GB normal. For the calculations discussed below, the fcc Al  $\Sigma 5$  [100]  $36.87^\circ$  twist GB (TGB) was used as the model system.

## 2. Theory

### 2.1. Thermodynamic framework

The thermodynamic foundations to a quantitative understanding of HID were laid roughly four decades ago, with the establishment of process rate dependent equations for the general problem of an impurity decorated GB subjected to uniaxial tensile stress [17, 18]. In the limits of both slow and fast fracture, determination of

the ideal work  $2\gamma_{\text{int}}$  of reversibly separating the two grains was shown to require information from the extreme points of the fracture process only. In other words, the sole GB related contribution to this quantity would involve the zero-load configurations. This conclusion reflects the loading response of the conjugate variables  $(\mu, \Gamma)$  – the impurity chemical potential and its surface density, respectively. In the fast fracture limit, any impurity influx to the GB is effectively suppressed (i.e.,  $\Gamma$  is fixed), while at the other extreme, the entire system remains in thermodynamic equilibrium (fixed  $\mu$ ). Generally, these parameters should be determined with reference to the *GB vicinity* – the GB region of influence from the perspective of the impurity.  $\Gamma$  is defined as the number of impurity atoms present in this region, divided by the area of the intersection with the (2D) GB plane. The chemical potential value immediately outside the vicinity is  $\mu$ . As the H mobility in metals is often considerable at ambient conditions [19], it is questionable if either of the above limits can be applied to this case [17]. When impurity mobility and crack speed are comparable, both  $\mu$  and  $\Gamma$  would be expected to vary during the fracture process [18], reflecting the system attempt to preserve chemical equilibrium when the GB displays an evolving ability to attract impurities. Here, an efficient modelling requires both a multi-scale scheme [14, 20, 21] and a careful atomistic examination of the impurity decorated GB structure over the full loading range to fracture. For a presumed homogeneous medium,  $2\gamma_{\text{int}}$  is identical to the Griffith-Irwin energy release rate, the work required to elastically advance a crack [22, 23, 7].

From the atomistic perspective, full information on HID in a uniaxial tensile test may be obtained by assessing the H influence on the *GB traction-separation (T-S) curve*, i.e., the variation in the GB cohesive stress  $\sigma$  with the separation (elongation) of the grains  $\delta$ . When this curve is integrated over the range of GB separations to complete fracture (noninteracting separated grains,  $\sigma = 0$ ), and with breakage being ‘ideal’, presumed occurring at the value of  $\delta$  where it becomes thermodynamically preferred,  $2\gamma_{\text{int}}$  results [18]. In addition, the entire stress-strain evolution is highlighted, especially the maximum (‘critical’) stress  $\sigma_c$  that the GB can withstand. Such investigations are well-established [24] within the density functional theory (DFT) framework [25, 26], where the GB vicinity is approximated via a GB supercell. However, the isolated supercell calculations are concerned with the strictly local GB response, in accordance with [27]. In other

words, the parameters  $\mu$  and  $\Gamma$  are ‘external’, and in the absence of multi-scale modelling, one must resort to approximations for their values.

The only two cases straightforwardly addressed involve constant values for either  $\mu$  or  $\Gamma$  during the full fracture process [18]. In the limit of slow fracture, at fixed temperature  $T$ , the GB cohesive stress is obtained as

$$\sigma = (1/A)(\partial\Omega/\partial\delta)_{T,\mu}, \quad (1)$$

while in the limit of fast fracture

$$\sigma = (1/A)(\partial G/\partial\delta)_{T,\Gamma}. \quad (2)$$

In these equations,  $A$  is the GB area for the system under investigation while  $\Omega$  denotes the grand canonical potential for the GB vicinity, related to the Gibbs free energy  $G$  by

$$\Omega = G - \mu A\Gamma. \quad (3)$$

Generally, *ab initio* simulations neglect the conjugate variable terms  $-TS$  and  $PV$ , replacing  $G$  by the internal energy  $E$ . This work adopts the same strategy. A full incorporation of the pressure-volume ( $PV$ ) term would require that a self-consistent structural coupling to the stress field in the surrounding grains be made [18].

For the temperature-entropy ( $TS$ ) term, configurational entropy changes (expected weak) could be formally included in zero-temperature studies. Evidently, Eq. (1) and (2) represent special cases, but they are shown in the present work to play a central role also when discussing fracture processes beyond the slow and fast limits.

For the isolated supercell study, the main aim is to quantify the evolving ability of the GB to attract H. This information is contained in the impurity formation energy,  $E_{\text{H}}^f(i)$ , i.e., the energy required to take the H atom from its presumed initial state as part of an environmental  $\text{H}_2$  molecule and onto a site  $i$  at the GB. For a chosen H surface density  $\Gamma_0$  compatible with practical simulation,

$$E_{\text{H}}^f(i, \Gamma_0, \delta) = E(i, \Gamma_0, \delta) - E(\delta) - \frac{1}{2}E(\text{H}_2) - \mu^*. \quad (4)$$

In Eq. (4), the first two energies on the right-hand side denote internal energies for a system hosting one GB, with only the former cell incorporating H. The chemical potential value  $\mu^*$  is computed relative to  $E(\text{H}_2)$  – the energy of an isolated  $\text{H}_2$  molecule. In the dilute limit (isolated H), every impurity atom added on a site  $i$  binds with the same energy, so for a given H surface density  $\Gamma$  within this range,  $E_{\text{H}}^f(i, \Gamma, \delta) = (\Gamma/\Gamma_0)E_{\text{H}}^f(i, \Gamma_0, \delta)$ . For the sake of simplicity, this limit was presumed throughout the present work. Accounting for configurational entropy, the theoretical surface density at site  $i$  in the slow fracture limit,  $\Gamma_i$ , can be computed for such noninteracting H as:

$$\Gamma_i = (N_i/A)\zeta_i/(1 + \zeta_i), \quad (5)$$

$$\zeta_i = \theta_{\text{H}} \times \exp(-E_s^0(i)/k_B T). \quad (5a)$$

In this Langmuir-McLean equation,  $N_i$  denotes the number of sites  $i$  available within the GB vicinity. The quantity  $\theta_{\text{H}}$  describes the H occupancy rate (atoms per site) in the bulk lattice, while  $E_s^0(i, \Gamma_0, \delta)$  is the H segregation energy at GB site  $i$ , at the condition specified. This energy is obtained from  $E_{\text{H}}^f(i, \Gamma_0, \delta)$  by subtracting the formation energy of an isolated H atom in the bulk lattice. If the picture of H segregation at the GB is extended to allow for simultaneous occupancy on several sites (but still with each H isolated), an expression for the internal energy may be constructed [28] from Eq. (4):

$$E(\Gamma, \delta) = E(\delta) + \sum_i (\Gamma_i/\Gamma_0)[E_{\text{H}}^f(i, \Gamma_0, \delta) + \frac{1}{2}E(\text{H}_2) + \mu^*], \quad (6)$$

with

$$\Gamma = \sum_i \Gamma_i. \quad (6a)$$

For the simulations of this work, the GB vicinity hosts one H atom, leading to  $\Gamma_0 = 1/A$ . Combining Eq. (6) and (3), it follows that the grand canonical potential in this scenario reads

$$\Omega(\Gamma, \delta) = E(\delta) + \sum_i (\Gamma_i/\Gamma_0)E_{\text{H}}^f(i, \Gamma_0, \delta). \quad (7)$$

It is emphasised that both Eq. (6) and (7) apply outside the slow fracture limit: this conclusion highlights how the supercell studies are technically decoupled from considerations defining the appropriate values for the H surface density and chemical potential.

## 2.2. Model system and computational details

The GB structure examined in the present work is the fcc Al  $\Sigma 5$  [100]  $36.87^\circ$  TGB. The supercell used for the description of this system is shown in Fig. 1. The GB nomenclature implies that the two grains differ in orientation by a rotation of  $36.87^\circ$  around the [100] axis, which is the normal vector to the GB plane ('TGB'). The labelling  $\Sigma 5$  is directly linked to the rotation angle: it emphasises the existence away from the GB of a substructure of fixed orientation. For a  $\Sigma 5$  GB, the atom density in this 'coincidence site lattice' (CSL) has been reduced by a factor 5, compared to the real bulk lattice. The CSL forms the logical basis of the GB supercell construction. It may be shown that the CSL basis vectors are related to the conventional fcc unit cell basis vectors in one grain as  $\{(1,0,0); (0, 3/2, 1/2); (0, -1/2, 3/2)\}$ , where the first vector points along the GB normal. Consequently, each (10 atom) CSL unit cell has dimensions  $\sqrt{5}a_{\text{Al}}/\sqrt{2}$  ( $a_{\text{Al}}$ ) in (out of) the GB plane, with  $a_{\text{Al}}$  denoting the fcc Al lattice parameter. Since the grains of the chosen GB supercell are volume filling, periodic boundary conditions require that two GBs be present. In connection with Eq. (4), this means that the energies  $E(i, \Gamma_0, \delta)$  and  $E(\delta)$  refer to half a supercell energy. Following earlier studies of the H-free Al  $\Sigma 5$  [100] TGB [27], a 40 atom cell was found to be sufficient for a converged atomistic T-S curve. For the sake of simplicity, the same cell was used throughout this work.

All calculations have employed DFT, using the projector augmented-wave method [29] as implemented in the plane wave (PW) based Vienna *Ab initio* Simulation Package (VASP) [30]. The exchange-correlation functional was described in the Perdew-Burke-Ernzerhof generalised gradient approximation [31]. For efficient convergence via formal introduction of partial occupancies in the calculations, the Methfessel-Paxton approach of order 2 [32] was chosen, with a smearing parameter of 0.1 eV. A 400 eV cut-off for the PWs and a  $7 \times 18 \times 18$  Monkhorst-Pack  $k$ -point grid [33] was found to provide convergence to the level of meV/GB for the H-free system. The H decorated GB investigations always involved one impurity atom at each GB in the cell. These H atoms were generally deposited on equivalent sites  $i$  and in different grains. At zero load, the impurity-free system was fully relaxed, producing cell dimensions of 6.37 Å (16.83 Å) in (normal to) the GB plane. The H influence on the cell dimensions was neglected throughout, resulting in  $\Gamma_0 =$

$2.5 \times 10^{-2} \text{ \AA}^{-2}$ . During configuration optimisation, all atomic coordinates in the cell were relaxed, with a force tolerance of  $1 \text{ meV/\AA}$ . The selected convergence tolerance in the electronic self-consistency loop was  $10^{-4} \text{ eV/cell}$ . The conjugate gradient algorithm was used throughout, with the importance of this choice over the Quasi-Newton algorithm emphasised by the observation of qualitative differences in the configuration predictions. Stress tensors for the construction of the H-free GB T-S curve were determined using the Nielsen-Martin scheme [34]. The H induced contributions to the tensile stress may be obtained in the same manner, or from the calculated impurity formation energies and their fitted derivatives  $\partial E_{\text{H}}^f(i)/\partial \delta$ , using Eq. (1) and (7).

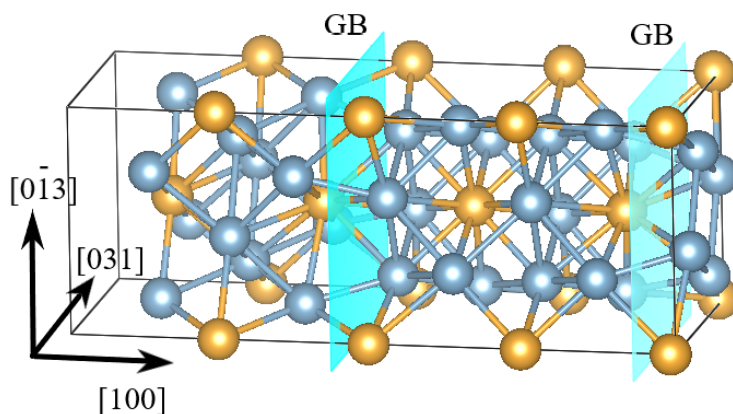


Fig. 1. Schematic presentation of the face-centred cubic Al  $\Sigma 5$  [100]  $36.87^\circ$  twist grain boundary supercell. Both grain boundaries in the cell have been highlighted, along with the (yellow) atoms of the coincidence site lattice substructure to which the cell periodicity makes reference. The basis vectors for this substructure are expressed in units of the basis vectors for the central grain.

In addition to the GB studies, the energies of a lone H atom in the bulk lattice and an isolated  $\text{H}_2$  molecule are necessary for the equations of Sec. 2.1 to be applied. For the latter investigation, a cell the size of  $4 \times 4 \times 4$  fcc Al conventional unit cells was found to eliminate interactions between periodic images in the  $\Gamma$ -point calculation, leading to the energy  $-3.379 \text{ eV/H atom}$ . For the study involving H in bulk Al, a single H atom

was placed at the preferred [35] tetrahedral (T) site in a 20 atom Al supercell based on two CSL unit cells stacked along the GB normal. This arrangement produced the same artificial H concentration as used for the GB studies. Once again, only the atomic coordinates were relaxed upon H insertion, with the cell dimensions referring to fully relaxed fcc Al. A  $14 \times 18 \times 18$   $k$ -point grid, compatible with the GB studies, was selected. Using Eq. (4), a H formation energy of 0.716 eV resulted, within 0.03 eV of the value reported by Wolverton *et al.* in [35]. The expected computational accuracy with this set-up is discussed in Sec. 3.3.

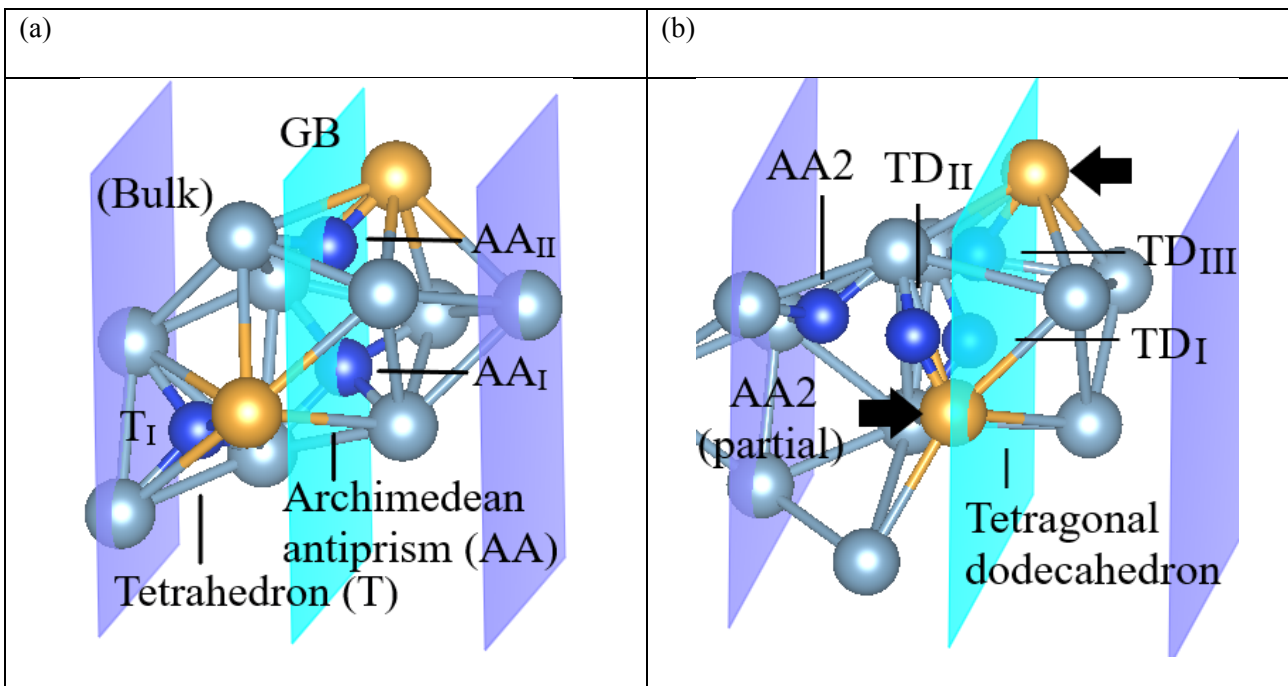


FIG. 2. Computed tensile stress response of the face-centred cubic Al  $\Sigma 5$  [100] twist grain boundary structure (key Al movements highlighted with arrows), and effect on the set of competitive H sites. (a):  $\delta = 0$  Å. (b):  $\delta = 1.5$  Å. H atom (dark blue spheres) positions are approximate, with impurity induced distortions suppressed throughout. For the sake of clarity, only selected atoms near the GB plane have been shown.

### 2.3. Tracking the H locations at the grain boundary

When performing an *ab initio* uniaxial tensile test on a GB free of impurities, it is recommended that the point of breakage be approached from the state of zero load via a sequential increase in  $\delta$  [14]. In this

‘dragged elongation’ scheme (DES), the atomic positions should be optimised for each chosen  $\delta$ . For a GB decorated with H, adopting the same strategy may produce incorrect answers, however. This is exemplified by the Al  $\Sigma 5$  [100] TGB, which undergoes a structural transformation during the loading stage, linked to the ‘bump’ on the T-S curve in [36]. This transition implies alterations (Fig. 2) to the GB characteristic set of polyhedral units [37], and in turn a modification of the set of competitive H sites. With the absence of dynamics in the DES, there is no guarantee that this scheme will reveal every relevant site generated. H relocation to a site clearly favoured at high loading may be prevented by the persistent presence of even weak energy barriers at each  $\delta$ . Given this shortcoming, the DES has been accompanied by a study tailored to identify all sites at GB separations *above* the structural transformation ( $\delta \geq 1.35$  Å). Starting from an identification of all competitive H sites at  $\delta = 1.5$  Å, the new investigation initiates both a DES and a ‘gradual compression’ scheme (GCS) at this GB separation for each relevant configuration. The latter scheme is reverse in nature to the original DES, probing H relocations upon a sequential reduction in  $\delta$  towards 0 Å. The level of hysteresis (energy barrier influence) in the system can now be probed as the difference between the GCS and original DES results for the respective sets of H configurations identified, as each scheme has the same basic limitation. Below, the original and new schemes will be referred to as the DES and DES-GCS, respectively.

### 3. Results and discussion

#### 3.1. Extension of the thermodynamic framework for GB atomistic elastic fracture modes

When introducing in Sec. 2.1 the thermodynamic framework appropriate for the present studies, the detailed appearance of the GB atomistic T-S curve was not discussed. This issue however is of interest in its own right, with Van der Ven and Ceder [14] showing how a computed T-S curve may host configurations that are not actually visited in the uniaxial tensile test. A correction of this flaw was shown to considerably reduce the computed value of  $\sigma_c$  for the case of cleavage in impurity hosting Al. The analysis in [14] did not pursue covering all ‘conceivable’ T-S curve shapes. Further, considerations surrounding cleavage at a low-index

plane do not take into account the possibility of breaking a subset of atomic bonds near or across the fracture plane on the route to complete fracture in the *ab initio* investigation. Such a feature may have direct influence on a GB T-S curve, as discussed in Sec. 2.3. It would therefore seem instructive to revisit the general consideration of [14], with focus on an attempted exhaustive set of T-S curves. For the sake of simplicity, the discussion below presumes the slow fracture limit, ideal breakage, and a GB hosting one impurity site only.

The analysis in [14] was centred on an inherent limitation to the T-S curve emerging from Eq. (1): The grand-canonical potential  $\Omega$  has  $\delta$  as a controlling variable, whereas it would be more physically sound to consider a thermodynamic potential that responds to a well-defined external stress  $\sigma$ . The grand-force potential  $\Phi$  satisfies this condition, being related to  $\Omega$  as

$$\Phi = \Omega - \delta(\partial\Omega/\partial\delta)_{T,\mu}. \quad (8)$$

Eq. (8) may be used to clarify if some of the configurations on the curve described by Eq. (1) actually remain unvisited in a realistic loading scenario. Such a situation arises if two stable configurations on this T-S curve are linked by the same cohesive stress, and if the work required to move between them at fixed stress is identical to the change in  $\Omega$ . In this case, Eq. (8) predicts *identical* values of  $\Phi(\sigma)$  for the two configurations, implying that the real transition occurs at constant stress  $\sigma_t$  (black curve in Fig. 3). If the GB in question is free of impurities, it transforms instantly as  $\sigma_t$  is reached. Otherwise, the transition may involve an impurity influx, with the duration controlled accordingly.

Since the two configurations connected by the transition stress  $\sigma_t$  are both mechanically stable, it follows that (i) the hypothetical part of the T-S curve in the intermediate range must involve a local stress maximum especially, and (ii) the GB cohesive stress will rise once the transition is completed. In other words, the corrected T-S curve is able to withstand an external stress higher than  $\sigma_t$ , but only beyond the transition stage. If the GB cohesive stress keeps rising from here, the strength of the atomic bonds across the GB plane will ultimately decrease to the point of breakage being triggered by thermal activation [36, 38]. The GB separation  $\delta_c$ , by construction the point where the critical stress is reached, hence will be the highest value

attainable for the intact GB – the ideal breakage point in the present simplified analysis. It may be (see Fig. 3) that the value of  $\sigma_c$  thus obtained falls below the prediction (for a hypothetical configuration) by Eq. (1).

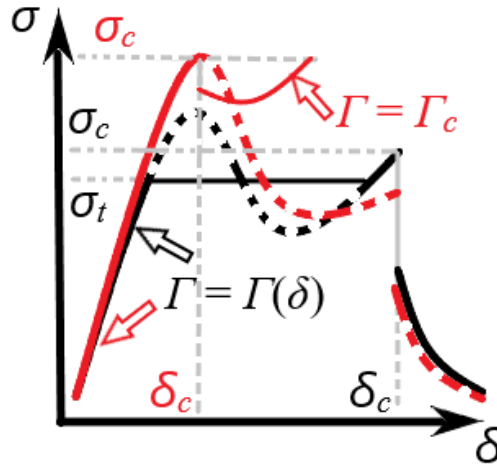


Fig. 3. Schematic illustration of two different impurity decorated grain boundary traction-separation curves (broad lines) predicted by Eq. (1), and their required modification (thin lines) in a realistic loading scenario. Dashed lines denote segments replaced in each correction procedure. Note that the breakage point for the corrected red curve is unknown.

Up to this point, the present analysis has rather closely followed [14]. However, a different scenario unfolds if the local stress maximum dismissed in the above discussion is actually real (as e.g. the red curve in Fig. 3). If this maximum is visited, the associated value *defines*  $\sigma_c$ , since a  $\sigma_t$  can always be found otherwise. Consequently, the GB is destined to break when the external stress rises above this local stress maximum. For an impurity-free system, breakage occurs instantly. The minimal work required (no heat loss) is connected to the area under the  $\sigma(\delta)$  curve for  $\delta > \delta_c$ . When added to the work associated with reaching the critical stress, the ideal work of reversibly separating the H-free grains  $(2\gamma_{\text{int}})_0$  results. For an impurity decorated GB, the analysis is fundamentally altered, reflecting that  $\Omega$  and  $G$  are no longer equivalent thermodynamic potentials. The T-S curve based on Eq. (1) describes a formally slow fracture limit also at  $\delta$

$> \delta_c$ , i.e. a hypothetical scenario where the GB vicinity always remains in chemical equilibrium with the surroundings. But the mechanical instability triggered at  $\delta_c$  physically induces a *fast* GB response, where the impurity influx and external stress changes can be neglected. It emerges that a transition must occur at  $\delta_c$  to the T-S curve associated with the fast fracture limit, Eq. (2), but with  $\Gamma = \Gamma_c (= \Gamma(\delta_c))$ , the impurity surface density at the onset of the instability. It is possible that the GB cohesive stress at  $\delta > \delta_c$  predicted with this curve will always remain below  $\sigma_c$ . In this case, the GB will still break instantly, but with  $2\gamma_{\text{int}}$  potentially differing from the prediction using Eq. (1). However, it may also happen (see Fig. 3) that mechanical equilibrium is re-established for the GB at some realistic value of  $\delta$ . In this case, breakage will be associated with a time delay. It remains ensured by the GB vicinity no longer being in chemical equilibrium with the surrounding grains, but depleted of impurities: any subsequent impurity influx will destabilise the GB according to Eq. (1), for which  $\sigma(\delta) < \sigma_c$  for  $\delta > \delta_c$ . But fracture is not triggered before reaching a system where mechanical stability can no longer be sustained, and the path to this point might require a considerable impurity influx.

Evidently, more complex T-S curve shapes than those pictured in Fig. 3 can be imagined. However, since the feature of potential interest to a discussion of curve reliability is always a local stress maximum, the analysis of the present section would appear exhaustive for the specified loading assumption. Thus, whenever the actual T-S curve of interest, obtained from Eq. (1), displays local features that places it in the category of the red curve in Fig. 3, two basic observations are made: (i) A correction is necessary, but cannot be constructed solely on the basis of this T-S curve, and (ii) the ultimate correction may be limited, as a varying  $\Gamma(\delta)$  will no longer be described by the Langmuir-McLean equation. A group of GB T-S curves exists, at least in principle, for which not even the slow fracture limit can be solved without the use of multi-scale modelling.

The mechanisms connected with this type of GB response are labelled below as ‘early critical stress’ for  $\sigma_c$  and ‘local delayed fracture’ for the subcategory where  $\Gamma$  evolves for some range of  $\delta > \delta_c$ . To the knowledge of the authors, such atomistic features have not been proposed previously in the literature at the theoretical level. The emphasis on locality for the second term is required in order to distinguish from the well-established [39] (macroscopic) delayed fracture, a central feature of H embrittled materials. The name

overlap seeks to emphasise the similarity of the two phenomena: in both cases, the external stress is fixed, with system breakage triggered by H diffusion to the ultimately fracturing region.

### 3.2. H sites and formation energies

The search for favourable H sites at the fcc Al  $\Sigma 5$  [100] TGB was limited to the region within two atomic layers of the GB plane (i.e., between the dark blue planes of Fig. 2(a)). This choice incorporates all polyhedral units sharing faces with at least one unit foreign to the bulk lattice, thereby attempting to filter out the full environment unique to the GB in question. At zero load, this region hosts six inequivalent geometries, with only one unit – the Archimedean antiprism (AA) [37] – standing out from the bulk. In calculations, all geometries were found to host local energy minima for H, but outside the AA, only one site was found to bind the impurity relative to fcc Al. The DES focussed on the sites within 0.2 eV of the most favourable configuration (a total of three configurations), thereby excluding one site in the AA. Since the GCS initiated at  $\delta = 1.5 \text{ \AA}$  suggested that the three most favourable configurations identified here transformed to the zero-load set upon unloading, the DES-GCS results described below highlighted these configurations only. Additional configurations of potential interest are mentioned in passing.

Fig. 4 shows the computed H formation energies according to the two schemes. The analysis has covered a range of GB separations including the impurity-free GB ideal breakage point ( $\delta = 2.15 \text{ \AA}$  [36]). For each configuration examined in the DES,  $E_H^f$  displays a monotonic decrease with  $\delta$ . The preferred H sites remain in the same geometry throughout the loading process (see Fig. 2), but the geometry itself is changing, from the AA in Fig. 2(a) to a tetragonal dodecahedron (TD) in Fig. 2(b). The impurity atoms relocate in response, occupying interstitial sites ( $AA_I$ ,  $AA_{II}$ ) at low loading, but moving to B type sites ( $TD_I$ ,  $TD_{II}$ , and  $TD_{III}$ ) as breakage is approached. This behaviour is in accordance with the expectations from [16]. The relative stability of the different sites is strongly affected by the tensile stress, indicating a general need for examining more than one site. Further, only the DES-GCS reveals the most favourable site at high loading,  $TD_{III}$ . These results emphasise the expected general usefulness of a combined DES and DES-GCS analysis

for H decorated metal GBs subjected to loading. Hysteresis is prominent in Fig. 4, with, e.g., the DES predicting a H movement from the best T site,  $T_I$ , to a site in a *different* AA geometry, AA2 (see Fig. 2(b)). In the GCS analysis, H was found to move back to  $T_I$  from this AA2 site. As the  $TD_{II}$  site represented an energetically more favourable choice for the same evolution, the AA2 site was neglected in Fig. 4(b). Dynamical simulations, beyond the scope of this work, would be required to quantify the influence of such metastable configurations, including the ease of transition to the  $TD_{III}$  site. Quantification of the H diffusion through and along a metal GB is an issue central to realistic larger scale modelling of HE [9]. Recent simulations have reported a significant  $T$  sensitivity for the diffusion coefficient at selected structurally simple GBs in Fe [40]. This result in turn suggests that H diffusion at the Al  $\Sigma 5$  [100] TGB may be appreciably affected by tensile stress in the slow fracture limit.

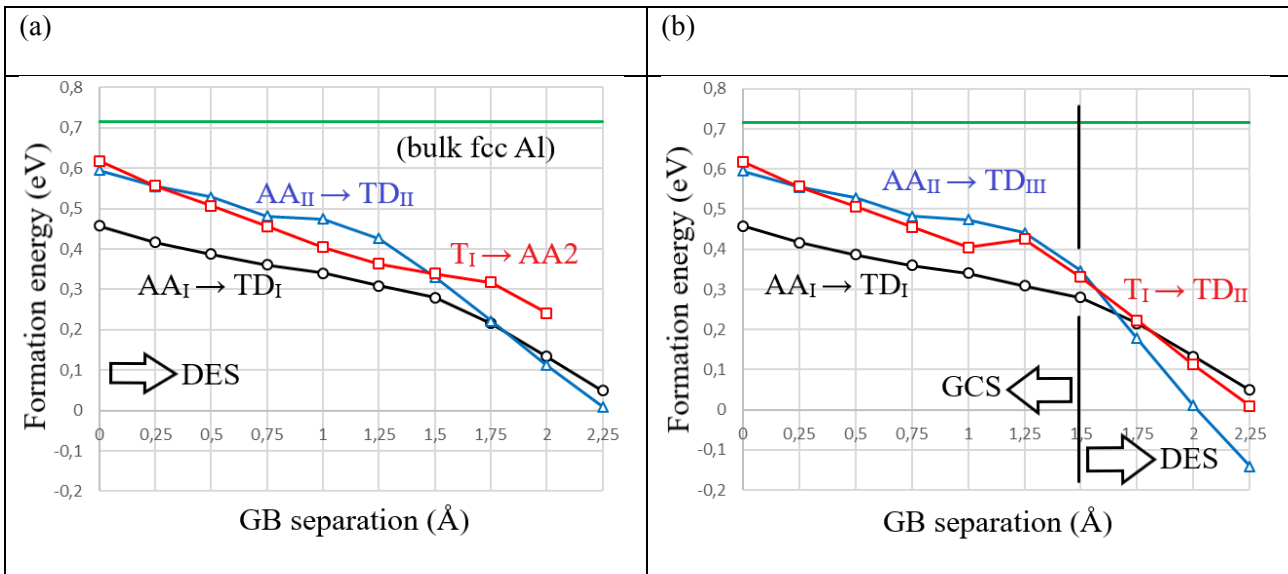


FIG. 4. Calculated H formation energies ( $\mu^* = 0$  eV) at the face-centred cubic Al  $\Sigma 5$  [100] twist grain boundary structure, obtained using (a) the DES (initiated at  $\delta = 0$  Å) and (b) the DES-GCS (initiated at  $\delta = 1.5$  Å). Quantitative differences are noted.

TABLE 1. Optimised H positions and associated formation energies ( $\mu^* = 0$  eV) for selected fcc Al  $\Sigma 5$  [100] twist grain boundary configurations in the uniaxial tensile test. The site nomenclature is explained in Fig. 2.

The vector  $\Delta S$  denotes the level of shear on the relaxed system. Two H atoms are present in the supercell, with the symmetry operations SO1, SO2 specifying the connection between the positions for the tabulated configurations. SO1:  $(x, y, z) \leftrightarrow (x+1/2, -z, -y)$ ; SO2:  $(x, y, z) \leftrightarrow (x+1/2, -y, z)$ .

Site	$\delta / \text{\AA}$	H coordinates	$\Delta S / \text{\AA}$ (in GB plane)	$E_{\text{H}}^f(\Gamma_0) / \text{eV}$
AA <sub>I</sub>	0.0	(0.437, 0.000, 0.500) (+ SO1)	(0.000, 0.000)	0.458
AA <sub>II</sub>	0.0	(0.437, 0.360, 0.650) (+ SO2)	(0.637, 0.000)	0.595
T <sub>I</sub>	0.0	(0.318, 0.313, 0.594) (+ SO1)	(-0.013, -0.013)	0.618
AA <sub>I</sub>	1.0	(0.438, 0.000, 0.500)	(0.000, 0.000)	0.341
T <sub>I</sub>	1.0	(0.306, 0.304, 0.599)	(-0.012, -0.012)	0.405
AA <sub>II</sub>	1.0	(0.459, 0.416, 0.671)	(0.147, 0.000)	0.475
TD <sub>I</sub>	1.5	(0.400, 0.000, 0.500) (+ SO1)	(0.000, 0.000)	0.280
TD <sub>II</sub>	1.5	(0.3827, 0.294, 0.514) (+ SO1)	(-0.170, -0.170)	0.331
AA2	1.5	(0.298, 0.297, 0.603) (+ SO1)	(0.023, 0.023)	0.339
TD <sub>III</sub>	1.5	(0.487, 0.491, 0.745) (+ SO2)	(0.880, 0.000)	0.347
TD <sub>III</sub>	2.0	(0.475, 0.561, 0.748)	(0.933, 0.000)	0.011
TD <sub>II</sub>	2.0	(0.390, 0.323, 0.520)	(-0.334, -0.334)	0.112
TD <sub>I</sub>	2.0	(0.372, -0.002, 0.552)	(-0.593, -0.593)	0.134
AA2	2.0	(0.301, 0.291, 0.647)	(0.457, 0.457)	0.241

Table 1 displays selected configurations from Fig. 4. The symmetry operations (SOs) connecting the two H atoms in the supercell may be understood by noting that (i) all unit cells describing this GB have fourfold rotational symmetry around the GB normal, and (ii) the 40 atom cell of this work (Fig. 1) obeys the SO  $(x, y, z) \leftrightarrow (x+1/2, -y, z)$ . As more than one H pair may be associated with a given configuration in general, it may be asked if the chosen configurations are representative. The potential importance of this issue is emphasised by the small supercell size and the fact that all atoms in the cell are free to move upon structural relaxation.

Earlier studies [41] have suggested fcc Al  $\Sigma 5$  [100] TGB shear energy contours much weaker than the energy differences among the H configurations, implying that the impurity may dominate structural relaxation.

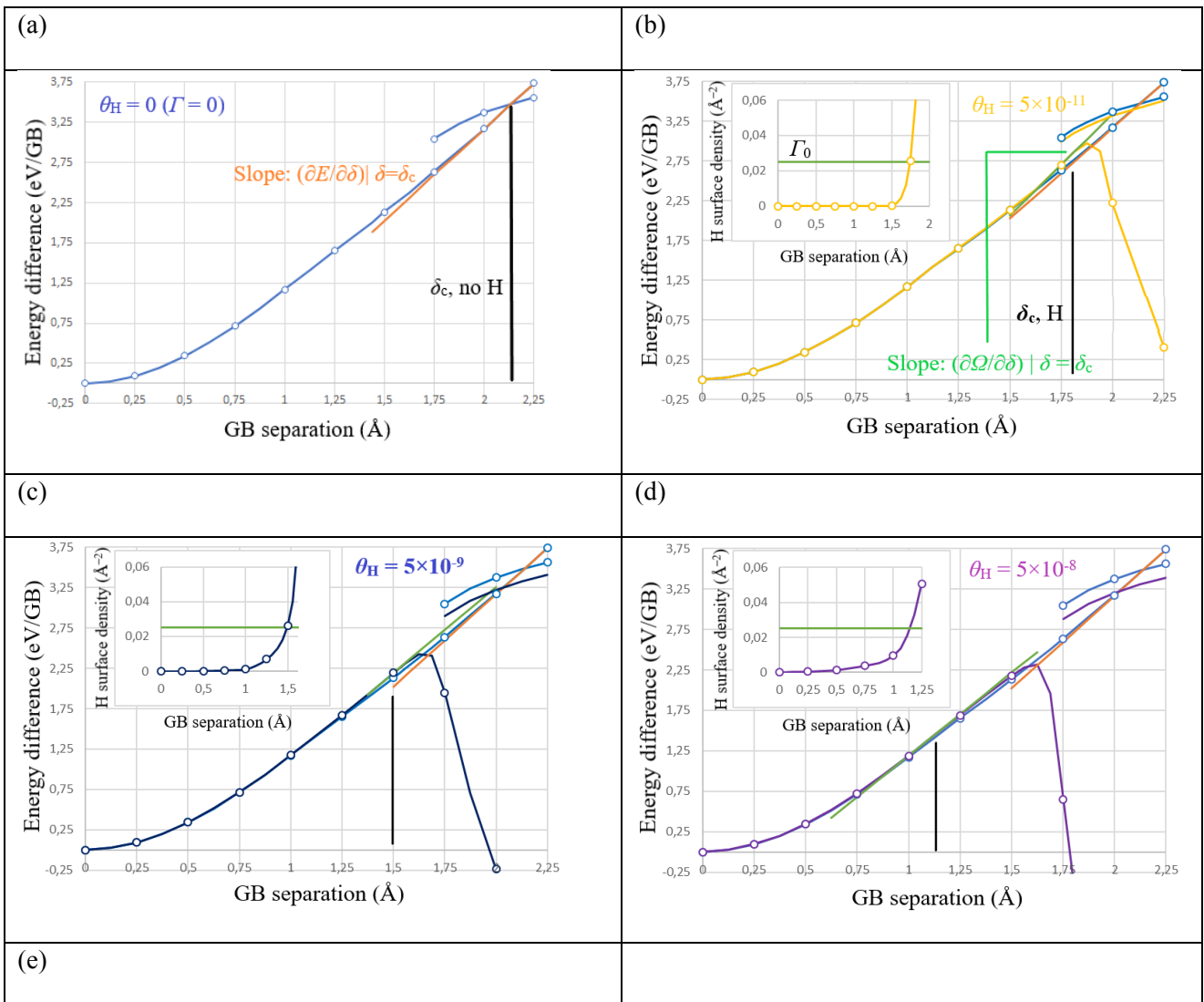
To address these issues, the H positions in Table 1 were corrected initially for any collective atom displacement during optimization. Subsequently, the level of shear was determined, as the H induced average relative displacement of the ‘bulk’ atoms (see Fig. 2) on either side of a grain. This feature,  $\Delta S$ , may indeed be prominent, with no obvious trends revealed. The influence on configuration energy scatter appears to be strongly dependent on tension. At  $\delta$  values below the GB structural transformation, energy differences for the AA<sub>II</sub> configurations (largest shear) based on SO1 and SO2 barely exceed 0.01 eV. By contrast, the corresponding difference for the TD<sub>II</sub> configuration at  $\delta = 2.25$  Å is roughly a factor higher. The reason for this evolution is unclear. It may be related to a reduced GB ability to accommodate structural distortion [41], or to H at TD sites causing larger structural disturbance. In Fig. 4, energy scatter connected with SOs has been suppressed to avoid mixing with energy changes due to configuration differences. It should be kept in mind that these two issues may be coupled, i.e. the choice of SO could promote a given H movement between sites. Further studies into SO influences are encouraged.

The selected H configurations in Fig. 4 do not represent all configurations binding the impurity. With increasing tensile stress, the geometries near the GB plane generally increase in volume. This leaves more room for the impurity, with beneficial effects for T sites especially. However, the same effect leads to easier diffusion of H onto sites in more open units (TD and AA2), as directly revealed for the configuration search at  $\delta = 1.5$  Å. Presumably, both behaviours are general, implying that configurations excluded from Fig. 4 should be of only little relevance.

### 3.3. Atomistic fracture modes

For all realistic bulk concentrations, H in Al may be described essentially as an ideal solution, with the relation between  $\theta_H$  and  $\mu^*$  outlined in [42]. Table 2 presents estimated values for the chemical potential used in this work. Within this range, at  $T = 300$  K, the fcc Al  $\Sigma 5$  [100] TGB remains H-free at zero load. This is

consistent with the experimental reports [15] of no detectable H segregation at GBs in pure Al under this condition. The result renders the fast fracture limit trivial: since the GB is H-free at the onset of loading, it will remain so at all stages of the uniaxial tensile test. Hence, only the slow fracture limit is discussed below. For the determination of  $\Omega$  to be free of ambiguities, the transition barriers in Fig. 4 were neglected, allowing H occupancy on each given site in accordance with Eq. (5) at each GB separation.



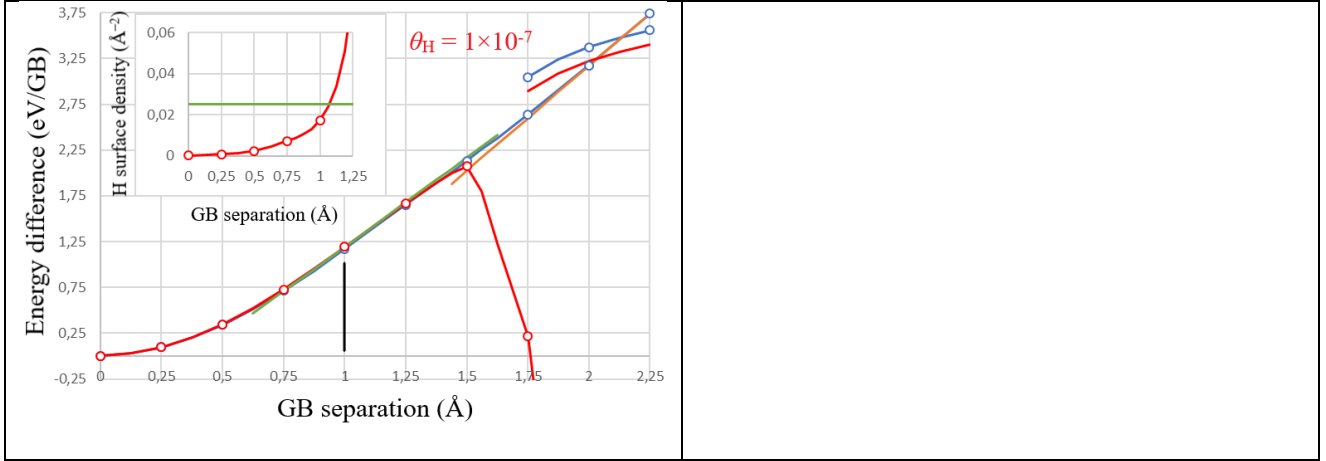


FIG. 5. Computed  $\Omega$  curves for various H decorated face-centred cubic Al  $\Sigma 5$  [100] twist grain boundaries, as obtained from Eq. (7), assuming thermodynamic equilibrium for each intact GB configuration and with  $\mu^*$  specified in Table 2. The H-free GB result in (a) ( $\Omega = E$ ) has been included in each figure for the sake of comparison. The full lines connecting open data points are guides to the eye. The inset shows H surface densities for the respective conditions. Separated grain energies in the presence of H (with  $\Gamma = \Gamma_c$ ) are estimated for all but the limit of large  $\delta$ .

Fig. 5 shows the results obtained (energies relative to the H-free GB at zero load) for four selected H bulk occupancy rates;  $\theta_H = 5 \times 10^{-11}$ ,  $5 \times 10^{-9}$ ,  $5 \times 10^{-8}$ , and  $1 \times 10^{-7}$ . The equivalent  $H_2$  pressures for these conditions are all rather high [43], ranging from 2 to 7 GPa according to [42]. As clarified below, these examples nonetheless are sufficiently representative for conclusions on the general behaviour of the system under the influence of H in the slow fracture limit to be made. For the H-free system ( $E(\delta)$  from Eq. (7)), both the intact GB and the separated grain configuration energies have been computed [36], in accordance with the scheme of [14]. The separated grain energies for H decorated systems were generally approximated for the sake of simplicity, based on the H formation energy at the most favourable site in the limit of large  $\delta$ . It was presumed that (i) this value of  $E_H^f$  remained unaffected as the grains were moved closer together. Further (ii),  $\Gamma$  was set equal to  $\Gamma_c$ , independent of GB separation. At  $\delta = 4 \text{ \AA}$ , H was found to strongly prefer a B type site on the exposed [100] surface, with a location between adjacent Al atoms in the surface plane. This result is in accordance with expectations from [16], as the Al-Al separation of  $2.86 \text{ \AA}$  provides sufficient space for such

a site. At  $\mu^* = 0$  eV, the computed value of  $E_H^f$  for this configuration was 0.102 eV. With no H present, 1.75 Å represents the lowest GB separation where a separated grain configuration remains stable [36]. This limit may be affected by the impurity if  $\Gamma$  rises to appreciable values.

A notable general feature for the  $\Omega$  curves in Fig. 5 is the ultimate sharp drop to negative values. Evidently, this behaviour is linked to the H formation energies in Fig. 4 decreasing monotonically, with the H influx ultimately causing a GB ‘collapse’ (compare with e.g. [14]). The physical aspects of this result are different, as discussed later in this section. A rigorous analysis of the H destabilisation starts out from Eq. (7) and (1), from which the analytic H contribution to the GB cohesive stress,  $\Delta\sigma_H$ , is obtained as:

$$\Delta\sigma_H(\delta) = \sum_i (1/A)(\Gamma_i/\Gamma_0)(\partial E_H^f(i)/\partial\delta)[1 - E_H^f(i)/((1 + \zeta_i)k_B T)]. \quad (9)$$

Since  $\partial E_H^f(i)/\partial\delta < 0$  in general, this expression reveals that H actually *stabilises* the GB at sufficiently low GB separations, where  $\zeta_i \ll 1$  and  $E_H^f(i)$  is well above 0.025 eV ( $k_B T$ ) for all  $i$ . As the tensile stress grows, perpetually more H is binding at the GB, and as  $E_H^f(i)$  for the dominant terms in Eq. (9) move sufficiently close to 0.025 eV, the number in the square brackets for these terms changes sign, resulting in the H contribution to the GB cohesive stress turning negative. With increasing  $\theta_H$  (decreasing  $\mu^*$ ), this turning point moves to lower GB separations as  $\Gamma_i$  rises and  $E_H^f(i)$  is lowered. Simultaneously,  $\Delta\sigma_H$  displays an increasingly modest variation around its zero value, effectively ‘pushing’ the highest  $\Omega$  slope, and thus  $\sigma_c$ , to  $\delta$  values far below the point where  $\Omega$  starts decreasing dramatically. This conclusion is not immediately noticeable in Fig. 5.

The appreciable sensitivity for the quantities  $\delta_c$  and  $\sigma_c$  to changes typically hardly visible in Fig. 5 imply that a rather dense set of  $(\delta, \Omega)$ -values is required to ensure an accurate T-S curve determination. While the extensive simulations of this work are expected to increase the reliability of the individual data points in Fig. 5 compared to standard (DES) analysis, the data point separation of 0.25 Å was found to be too wide for a reliable T-S curve construction to be accomplished. Estimated values for the critical stress (expected errors within 0.2 GPa) have been listed in Table 2, along with associated values of  $\delta_c$  and  $\Gamma_c$ , with Fig. 5 providing visualisation. These results indicate H stabilisation of the GB even for  $\theta_H$  reaching  $5 \times 10^{-11}$ . From this point

onwards, the impurity influence appears to become persistently less beneficial, with H induced reduction of the critical stress initiated before  $\theta_H = 5 \times 10^{-9}$ . This prediction concerning a mechanism in the line of HID appears in agreement with experimental findings: Stress induced H segregation at Al GBs has been reported in the literature, see [15], but, to the knowledge of the authors, H-induced intergranular embrittlement has not been observed in pure Al (with most analyses presumably involving  $\theta_H$  values below the range of Fig. 5).

TABLE 2: Computed [36] (H-free system) and estimated values for the critical stress, and the associated GB separation and H surface density for the systems of Fig. 5.

$\theta_H$ (site <sup>-1</sup> )	$\mu^*$ (eV)	$\sigma_c$ (GPa)	$\delta_c$ (Å)	$\Gamma_c$ (Å <sup>-2</sup> )
0	-	9.03	2.15	-
$5 \times 10^{-11}$	0.1255	10.1	1.81	0.058
$5 \times 10^{-9}$	0.2462	8.4	1.50	0.026
$5 \times 10^{-8}$	0.3065	8.1	1.13	0.021
$1 \times 10^{-7}$	0.3247	7.7	1.00	0.017

A second notable aspect in Fig. 5 is the absence of crossing intact GB and separated grain energy curves for the H containing systems. This feature implies a fundamentally changed loading response of the fcc Al  $\Sigma 5$  [100] TGB when H is present: In Fig. 5,  $\sigma_c$  always has the characteristics of an early critical stress, as defined in Sec. 3.1. Even for the least affected system examined ( $\theta_H = 5 \times 10^{-11}$ ), it seems questionable that a more accurate determination of the separated grain energies will change this conclusion by suggesting breakage by thermal activation at  $\delta < \delta_c$ . In addition to such breakage having to be thermodynamically favoured, H would also have to reduce an appreciable energy barrier to bond breakage across the GB plane present at this GB separation [36]. At the larger values of  $\theta_H$  in Fig. 5, breakage at  $\delta < \delta_c$  must seem impossible as the condition of a thermodynamically favoured process cannot be obeyed. Thus (see Sec. 3.1), presumably none of the computed  $\Omega$  curves can be applied for construction of the GB T-S curve at  $\delta > \delta_c$ . Rather, the stress

determination will require the computation of  $E(\Gamma_c, \delta)$  and use of Eq. (2) initially. This conclusion provides an explanation to the unphysical GB collapse involving negative  $\Omega$  values in Fig. 5. The evolution in the grand canonical potential merely reflects that chemical equilibrium is absent for the intact GB at  $\delta > \delta_c$ .

As argued in Sec. 3.1, instant breakage is not necessarily implied by the external stress rising above an early critical stress. The GB mechanical stability may be re-established if  $E(\Gamma_c, \delta)$  leads to a prediction of GB cohesive stresses exceeding  $\sigma_c$  at some realistic value of  $\delta$ . Mathematically, this local delayed fracture condition may be expressed as:

$$\sum_i (1/A)(\Gamma_{c,i}/\Gamma_0)(\partial E_H^f(i)/\partial \delta) \geq \sigma_c - \sigma_{\text{NO H}}(\delta). \quad (10)$$

In this inequality, the left-hand side describes  $\Delta\sigma_H$  for the case of a fixed H surface density, while the parameter  $\sigma_{\text{NO H}}$  denotes the H-free GB cohesive stress. A ‘frozen’ H atom distribution,  $\Gamma_i = \Gamma_{c,i}$ , has been assumed, reflecting that the GB response at this stage is likely too fast for even impurity relocation on the GB sites to occur. For the two lowest  $\theta_H$  values in Fig. 5, the GB sites are modified over the range of consideration, implying that the DES results of Fig. 4(a) should be used as input.

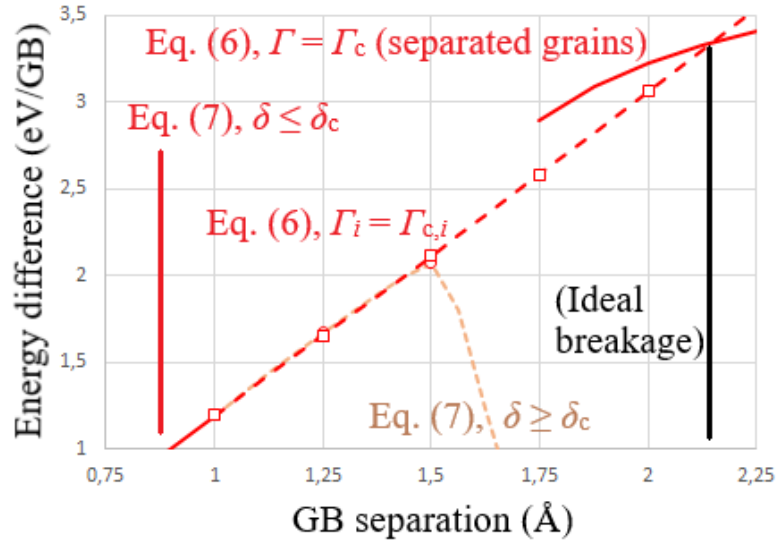


FIG. 6. Proposed correction to the computed slow fracture limit behaviour of the H decorated face-centred cubic Al  $\Sigma 5$  [100] twist grain boundary in Fig. 5(e). At  $\delta \geq \delta_c$  (1 Å), the dashed red curve  $E(\Gamma_c, \delta)$  replaces

the dotted brown  $\Omega$  curve, reflecting a fast system response once the critical stress  $\sigma_c$  has been exceeded. At the present H bulk concentration, this mechanical instability likely leads to instant breakage (see text for details).

Fig. 6 shows an example of an energy-separation curve, for the case  $\theta_H = 5 \times 10^{-9}$ , corrected according to the guidelines of Sec. 3.1. At  $\delta_c = 1 \text{ \AA}$ ,  $\Omega$  ideally should change continuously into  $E(\Gamma_c, \delta)$ , with the configuration at this GB separation representing a visited system in both the slow and fast fracture process. In practice, the curve energies are within 1 meV of each other, indicating a rather accurate estimation in Table 2. Following an initial drop,  $\partial E(\Gamma_c, \delta)/\partial \delta$  (interpolated) starts rising, moving within the estimated uncertainty on  $A\sigma_c$  above  $1.75 \text{ \AA}$ . This value is never exceeded, though, meaning that it remains unclear if the GB breaks instantly (as shown in Fig. 6) or with the aid of a H flux. At the lower  $\theta_H$  values examined in Fig. 5, the variation in  $\Gamma$  with GB separation is more pronounced, resulting in a larger uncertainty for the estimated  $E(\Gamma_c, \delta)$  curve. At these conditions, it is however generally evident that local delayed fracture is suppressed. Direct application of Eq. (10) requires a denser set of data points.

The accuracy in the predictions of this section largely rests upon the reliability of the H formation energy determination in Fig. 4. A common displacement of the  $E_H^f$  values appears to have little influence on the T-S curve predictions connected with Eq. (1). As an example, a non-negligible correction of 0.04 eV may reduce all  $\xi_i$  values by a factor 5 (see Eq. (5)), with similar consequences to  $\Gamma_i$  at the lower values of  $\delta$ . However, at  $\theta_H = 1 \times 10^{-7}$ , where the effect on  $\Omega$  is expected to be highest due to the comparatively gradual rise in H surface density (see Fig. 5), the predicted  $(\delta_c, \sigma_c)$ -values are hardly affected. It would seem defensible to suggest a rather weak influence of even the full set of errors encountered for  $\delta$  values below the GB structural transformation: In this range,  $\Gamma$  remains below  $\Gamma_0$ , and H primarily occupies the  $AA_1$  site where lattice relaxations were found to be weak. Beyond the transformation, errors are undoubtedly larger, due to reduced precision in the  $E_H^f$  determination of Fig. 4 (see Sec. 3.2) and the ultimate breakdown of the assumption of isolated H (see Sec. 2.1). The latter issue primarily affects predictions at low H concentrations, since  $\Gamma_c$  rises with decreasing  $\theta_H$  (Table 2). At the two highest  $\theta_H$  values considered in this

work, both sources of errors would seem rather unimportant, as  $\Omega$  has already decreased significantly for GB separations even weakly above  $\delta_c$ . Along with the conclusions concerning HID, the appearance of an early critical stress for most, if not all, H decorated fcc Al  $\Sigma 5$  [100] TGBs examined therefore seems a reliable result, within the chosen modelling limitations. The exact nature of breakage may be a different matter, as  $E(\Gamma_c, \delta)$  is generally strongly affected (via  $\Gamma_c$ ) by errors in Fig. 4.

### 3.4. Estimated H influence on $2\gamma_{\text{int}}$

For the thermodynamic considerations of Sec. 2.1, the slow and fast fracture limits represent the two examples where  $2\gamma_{\text{int}}$  is always independent of T-S curve features. From an atomistic perspective, both limits are idealisations. Even when the impurity can be considered essentially immobile during the fracture process, energy barriers to breakage connected with the atomistic nature of the system have been neglected [7, 38]. For the case of a mobile impurity, an additional source of error is present. As argued in Sec. 3.1, once the critical stress is exceeded, the breakage process will normally (excepting local delayed fracture) proceed via a fast reaction where the surface density is essentially fixed. For a physical loading scenario where mobile impurity effects are non-negligible there is thus no reason why, upon approaching the slow fracture limit, a newly exposed fracture surface should necessarily reach a state of chemical equilibrium with the bulk lattice. Rather, the expected surface density at this point would typically be equal to  $\Gamma_c$ , reflecting the last intact GB configuration normally visited. If breakage is immediate when the external stress  $\sigma$  exceeds  $\sigma_c$ , the chemical potential outside the GB vicinity may be presumed practically constant during the final stage  $\delta > \delta_c$ . It follows that, presuming ideal breakage,  $2\gamma_{\text{int}} (= \int \sigma d\delta)$  may still be determined using Eq. (1) with a modified grand canonical potential for the limit of large  $\delta$ . From Eq. (7),

$$(2\gamma_{\text{int}})_\mu = (2\gamma_{\text{int}})_0 + \sum_j (\Gamma_{c,j}/\Gamma_0) E_{\text{H}}^f(j, \Gamma_0, \infty) - \sum_i (\Gamma_i(\delta=0)/\Gamma_0) E_{\text{H}}^f(i, \Gamma_0, 0). \quad (11)$$

In this expression, all H influences on the right-hand side are contained in the two sums, with  $(2\gamma_{\text{int}})_0$  given as  $E(\infty) - E(0)$  within the approximation of the present work. The first sum runs over available fracture surface

sites, and by necessity must include an assumption for the impurity distribution (e.g. full equilibration in the GB vicinity). Eq. (11) was applied in Fig. 5.

The analysis of this work has shown that in the slow fracture limit, impurity induced GB destabilisation is directly linked (Eq. (9)) to a perpetually strengthened impurity segregation at the GB with increased  $\delta$ . For the H decorated fcc Al  $\Sigma 5$  [100] TGB,  $\Gamma$  ultimately rises drastically in accordance with the monotonic decrease in  $E_H^f(i)$ , see Fig. 5, but the critical stress is reached at the onset of this rise, mostly staying below  $\Gamma_0$ . As discussed in Sec. 3.3, the GB likely breaks instantly as  $\sigma_c(\theta_H)$  is exceeded, suggesting that the  $\Gamma_c$  values of Table 2 represent surface densities immediately after fracture at the given H occupancy rate. Notably,  $\Gamma_c$  is *decreasing* with increasing  $\theta_H$ . From Eq. (9), this behaviour can be related to the drop in  $E_H^f(i)$  with rising  $\mu$ : effectively, when the chemical potential outside the GB vicinity is raised, the destabilising effect of each H atom is growing. This conclusion is in marked contrast to the standard thermodynamic analysis avoiding GB T-S curve considerations. Here,  $\Gamma$  is estimated using Eq. (5), and since  $E_s^0(i)$  is unaffected by variations in  $\mu$ , the predicted surface density increases with  $\theta_H$ . Even though the present comparison involves one loading scenario only, it is evident that the two approaches to estimating  $(2\gamma_{\text{int}})_\mu$  described are fundamentally different. Table 3 substantiates this conclusion for the case of the Al  $\Sigma 5$  [100] TGB. Using data from earlier sections, the standard analysis is found to predict H-induced reductions typically more than an order of magnitude higher than the T-S curve-based estimate. Both sets of results comply with the rule of [18] that a mobile impurity reduces  $2\gamma_{\text{int}}$ .

The limitations of the above discussed standard analysis have been recognised in earlier work. Yamaguchi *et al.* [13] proposed that the maximum mobile H influence on  $2\gamma_{\text{int}}$  in a sustained load test could be determined as the GB area weighted sum over the H segregation energies when changing the H surface density from  $\Gamma(\delta = 0)$  into the value connected with chemical equilibrium at the given environmental condition. Leaving aside the technical differences to the slow fracture limit consideration, the estimate in [13] is noted to be identical to a standard analysis for the case of the Al  $\Sigma 5$  [100] TGB, since  $\Gamma(\delta = 0)$  is negligible for this system. More generally, the analysis in [13] appears to rest upon a presumed close similarity for the energy variation with  $\Gamma$  between the decohering GB and the fractured system, which has been put into question in this work as well

as in more general considerations [44]. A quantitative comparison with T-S curve-based predictions would require multi-scale modelling on the latter part as the sustained load test takes the GB vicinity out of chemical equilibrium with the bulk lattice at the outset.

TABLE 3. Computed ideal work  $(2\gamma_{\text{int}})_{\mu}$  of reversibly separating the H-decorated face-centred cubic Al  $\Sigma 5$  [100] twist grain boundary in the slow fracture limit according to two approaches: GB T-S curve analysis (this work) and standard estimation [18]. The corresponding work  $(2\gamma_{\text{int}})_0$  in the absence of H is equal to 1520  $\text{mJ/m}^2$  (3.84 eV/GB for the supercell examined [36]).

$\theta_{\text{H}}$ ( $\text{site}^{-1}$ )	$(2\gamma_{\text{int}})_{\mu} - (2\gamma_{\text{int}})_0, \Gamma_{\text{c}}\text{-based (mJ/m}^2)$	$(2\gamma_{\text{int}})_{\mu} - (2\gamma_{\text{int}})_0, \text{standard (mJ/m}^2)$
0	0	0
$5 \times 10^{-11}$	-22	-141
$5 \times 10^{-9}$	-59	-910
$5 \times 10^{-8}$	-68	-1290
$1 \times 10^{-7}$	-60	-1410

The analysis of this work has focused on a defect-free GB with no impurities present (alloying elements included) other than H. Motivated by experimental results, other computational studies have moved beyond this limitation [12, 45], addressing H-C and H-vacancy interactions with Fe GBs and proposing fundamentally different candidate mechanisms for H-induced delayed fracture. The scope of the present studies does not allow a meaningful criticism of these findings. It is however evident that even when presuming dominance of HID effects as a fundamental support for the relevance of *ab initio* tensile tests, the atomistic details of the mechanisms involved would presently remain a matter of dispute. It is possible that more than one proposed mechanism is relevant within its own set of systems. Nonetheless, a careful comparison of the different theories with experimental results for a system where each theory has potential credibility might be highly valuable for separating flawed and realistic hypotheses.

#### 4. Summary and outlook

Using the fcc Al  $\Sigma 5$  [100] TGB as a test system, the present DFT based study has attempted to clarify expected trends when allowing for an evolving H decoration of a metal GB subjected to a uniaxial tensile test, probing the slow fracture limit only. The H formation energies at this GB generally display a monotonic decrease with increasing GB separation as the favoured GB sites gradually change into B type sites. Further, the GB undergoes a structural transformation during loading, triggering H movements to new sites. For the full evolution to be reliably explored within a zero-temperature model framework, an additional starting point had to be introduced in the computational uniaxial tensile test, at  $\delta$  values above the GB transformation stage. Some of the energy barrier heights to H relocation are clearly low, as supported by weak loading-unloading hysteresis. In other cases, however, no information on this issue was obtained from the above study, indicating that a direct determination of transition barrier heights with the nudged elastic band method is required. These findings emphasise that for an impurity diffusing as easily as H and showing affinity for a wealth of GB sites, any single site model must appear inadequate.

The shape of the H decorated GB T-S curve may profoundly affect the system response in a uniaxial tensile test. If the critical stress  $\sigma_c$  occurs ‘early’, before the maximum achievable elongation on the intact GB is formally attained, the predicted GB evolution at  $\sigma > \sigma_c$  must be modified in recognition of thermodynamic equilibrium no longer being maintained even in the slow fracture limit. According to the simulations for the H decorated fcc Al  $\Sigma 5$  [100] TGB, such an early critical stress is likely present whenever the impurity non-negligibly affects the GB response. This is a direct consequence of the strong, monotonic decrease in the H formation energies with GB separation. For the test system, such effects require equivalent  $H_2$  pressures of at least a few GPa, with the impurity ultimately triggering HID as well in this range. It is possible that sufficiently high H bulk occupancy rates  $\theta_H$  will induce a transition for  $\sigma > \sigma_c$  to a configuration for which instability is ensured but triggered by a H influx. This ‘local delayed fracture’ scenario in general can only be fully described with multi-scale modelling. H was found to lower  $\sigma_c$  for the test system by up to 15%. The

estimated values of  $(2\gamma_{\text{int}})_{\mu}$  were clearly less affected, by 4.4% or less, in marked contrast to standard thermodynamic results.

The present analysis has not discussed the extent to which the above phenomena may be viewed as common features for H decorated metal GBs under realistic conditions. In this context, it appears intriguing that (i) the B type sites preferred by H for the chosen test system of this work emerge naturally at the GB with increasing tensile stress, and (ii) these sites bear a clear structural resemblance to the H sites in a metal hydride. For several metals [1], stress induced stabilization of hydrides has been reported, supporting in turn the possibility of prominent H segregation at B type sites for GBs subjected to significant tensile stress. Recent theoretical investigations have highlighted the stability of nanohydrides in a metal not normally viewed as being prone to hydride formation, see e.g. [46].

As noted above, multi-scale modelling may be required to fully characterize the T-S curve if the GB hosts an early critical stress. Further, it is a central objective of HID analysis to move beyond the slow fracture limit to scenarios involving comparable crack speed and impurity mobility. The key equations of the present work, Eq. (6), (7), (9), and (10), are all directly applicable for implementation in such schemes, assuming only mechanical equilibrium within the DFT model system. The H surface density and chemical potential appear in the model scheme as external parameters that may be directly adjusted in the attempt to simulate a changed loading rate.

## Acknowledgments

The calculations were performed using HPC resources from GENCI- [CCRT/CINES/IDRIS] (Grant 2016-[t2016097681]) and MAGI, the HPC cluster of SPC (Sorbonne Paris Cité) University. The authors thank N. Greneche for his support on MAGI. ANR (Agence Nationale de la Recherche) and CGI (Commissariat à l'Investissement d'Avenir) are gratefully acknowledged for their financial support through Labex SEAM (Science and Engineering for Advanced Materials and devices), ANR 11 LABX 086, ANR 11 IDEX 05 02

and through the funding of the MEMMI (Multi-scale modelling of materials and interfaces) project. Fig. 1, 2 were constructed using the VESTA software [47].

#### Data availability

The raw/processed data required to reproduce these findings cannot be shared at this time due to technical or time limitations.

#### References

- [1] S. M. Myers, M. I. Baskes, H. K. Birnbaum, J. W. Corbett, G. G. DeLeo, S. K. Estreicher, E. E. Haller, P. Jena, N. M. Johnson, R. Kirchheim, S. J. Pearton, and M. J. Stavola, Hydrogen interactions with defects in crystalline solids, *Rev. Mod. Phys.* 64 (1992) 559–617.
- [2] M. S. Daw and M. I. Baskes, Semiempirical, Quantum Mechanical Calculation of H Embrittlement in Metals, *Phys. Rev. Lett.* 50 (1983) 1285–1288.
- [3] W. Zhong, Y. Cai, and D. Tomanek, Computer simulation of H embrittlement in metals, *Nature* 362 (1993) 435–437.
- [4] L. Zhong, R. Wu, A. J. Freeman, and G. B. Olson, Charge transfer mechanism of hydrogen-induced intergranular embrittlement of iron, *Phys. Rev. B* 62 (2000) 13938–13941.
- [5] H. Vehoff and P. Neumann, Crack propagation and cleavage initiation in Fe-2.6%-Si single crystals under controlled plastic crack tip opening rate in various gaseous environments, *Acta Metall.* 28 (1980) 265–272.
- [6] M. B. Djukic, G. M. Bakic, V. Sijacki Zeravcic, A. Sedmak, and B. Rajcic, The synergistic action and interplay of hydrogen embrittlement mechanisms in steels and iron: Localized plasticity and decohesion, *Eng. Fract. Mech.* 21 (2019) 106528 (33pp).

- [7] J. R. Rice and J.-S. Wang, Embrittlement of Interfaces by Solute Segregation, *Mater. Sci. Eng. A* 107 (1989) 23–40.
- [8] O. Barrera, D. Bombac, Y. Chen, T. D. Daff, E. Galindo-Nava, P. Gong, D. Haley, R. Horton, I. Katzarov, J. R. Kermode, C. Liverani, M. Stopher, and F. Sweeney, Understanding and mitigating hydrogen embrittlement of steels: a review of experimental, modelling and design progress from atomistic to continuum, *J. Mater. Sci.* 53 (2018) 6251–6290.
- [9] S. Serebrinsky, E. A. Carter, and M. Ortiz, A quantum-mechanically informed continuum model of hydrogen embrittlement, *J. Mech. Phys. Solids* 52 (2004) 2403–2430.
- [10] X. J. Shen, D. Tanguy, and D. Connétable, Atomistic modelling of hydrogen segregation to the  $\Sigma 9$  {221}[110] symmetric tilt grain boundary in Al, *Philos. Mag.* 94 (2014) 2247–2261.
- [11] M. Yuasa, T. Amemiya, and M. Mabuchi, Enhanced grain boundary embrittlement of an Fe grain boundary segregated by hydrogen (H), *J. Mater. Res.* 27 (2012) 1589–1597.
- [12] H. Momida, Y. Asari, Y. Nakamura, Y. Tateyama, and T. Ohno, Hydrogen-enhanced vacancy embrittlement of grain boundaries in iron, *Phys. Rev. B* 88 (2013) 144107 (13pp).
- [13] M. Yamaguchi, K.-I. Ebihara, M. Itakura, T. Kadoyoshi, T. Suzudo, and H. Kaburaki, First-Principles Study on the Grain Boundary Embrittlement of Metals by Solute Segregation: Part II. Metal (Fe, Al, Cu)-Hydrogen (H) Systems, *Metall. Mater. Trans. A* 42A (2011) 330–339.
- [14] A. Van der Ven and G. Ceder, The thermodynamics of decohesion, *Acta Mater.* 52 (2004) 1223–1235.
- [15] G. A. Young Jr and J. R. Scully, The diffusion and trapping of hydrogen in high purity aluminum, *Acta Mater.* 46 (1998) 6337–6349.
- [16] F. Apostol and Y. Mishin, Hydrogen effect on shearing and cleavage of Al: A first-principles study, *Phys. Rev. B* 84 (2011) 104103 (5pp).

- [17] J. R. Rice, *Hydrogen and Interfacial Cohesion*, in: *Effect of Hydrogen on Behavior of Materials*, edited by A. W. Thompson and I. M. Bernstein, publication of The Metallurgical Society of AIME, New York (1976) 455–468.
- [18] J. P. Hirth and J. R. Rice, On the Thermodynamics of Adsorption at Interfaces as it Influences Decohesion, *Metall. Trans. A* 11A (1980) 1501–1511.
- [19] The room temperature H diffusivity in bulk fcc Al is approximately  $10^{-11}$  m<sup>2</sup>/s according to the most detailed analyses. Practical simulations in this work however involved the slow fracture limit, with the impurity hence automatically being treated as ‘highly mobile’.
- [20] I. H. Katzarov and A. T. Paxton, Hydrogen embrittlement II. Analysis of hydrogen-enhanced decohesion across (111) planes in  $\alpha$ -Fe, *Phys. Rev. Mater.* 1 (2017) 033603 (10pp).
- [21] Y. Mishin, P. Sofronis, and J. L. Bassani, Thermodynamic and kinetic aspects of interfacial decohesion, *Acta Mater.* 50 (2002) 3609–3622.
- [22] A. A. Griffith, The Phenomena of Rupture and Flow in Solids, *Phil. Trans. R. Soc. A* 221 (1920) 163–198.
- [23] G. R. Irwin, Analysis of Stresses and Strains Near the End of a Crack Traversing a Plate, *J. Appl. Mech.* 24 (1957) 361–364.
- [24] M. Yamaguchi, M. Shiga, and H. Kaburaki, Grain Boundary Decohesion by Impurity Segregation in a Nickel-Sulfur System, *Science* 307 (2005) 393–397.
- [25] P. Hohenberg and W. Kohn, *Phys. Rev.* 136 (1964) B864–B871.
- [26] W. Kohn and L. J. Sham, *Phys. Rev.* 140 (1965) A1133–A1138.
- [27] F. J. H. Ehlers, M. Seydou, D. Tingaud, F. Maurel, Y. Charles, and S. Queyreau, Supercell size convergence testing in uniaxial tensile test studies of an Al grain boundary: A proposed path to a robust analysis, *Comput. Mater. Sci.* 139 (2017) 39–47.

- [28] D. Udler and D. N. Seidman, Solute segregation at [001] tilt boundaries in dilute f.c.c. alloys, *Acta Mater.* 46 (1998) 1221–1233.
- [29] P. E. Blöchl, Projector augmented-wave method, *Phys. Rev. B* 50 (1994) 17953–17979.
- [30] G. Kresse and D. Joubert, From ultrasoft pseudopotentials to the projector augmented-wave method, *Phys. Rev. B* 59 (1999) 1758–1775.
- [31] J. P. Perdew, K. Burke, and M. Ernzerhof, Generalized Gradient Approximation Made Simple, *Phys. Rev. Lett.* 77 (1996) 3865–3868.
- [32] M. Methfessel and A. T. Paxton, High-precision sampling for Brillouin-zone integration in metals, *Phys. Rev. B* 40 (1989) 3616–3621.
- [33] H. J. Monkhorst and J. D. Pack, Special points for Brillouin-zone integrations, *Phys. Rev. B* 13 (1976) 5188–5192.
- [34] O. H. Nielsen and R. M. Martin, Quantum-mechanical theory of stress and force, *Phys. Rev. B* 32 (1985) 3780–3791.
- [35] C. Wolverton, V. Ozolins, and M. Asta, Hydrogen in aluminum: First-principles calculations of structure and thermodynamics, *Phys. Rev. B* 69 (2004) 144109 (16pp).
- [36] F. J. H. Ehlers, M. Seydou, D. Tingaud, F. Maurel, Y. Charles, and S. Queyreau, *Ab initio* determination of the traction-separation curve for a metal grain boundary: a critical assessment of strategies, *Modelling Simul. Mater. Sci. Eng.* 24 (2016) 085014 (17pp).
- [37] M. F. Ashby, F. Spaepen, and S. Williams, The structure of grain boundaries described as a packing of polyhedral, *Acta Metall.* 26 (1978) 1647–1663.
- [38] Z. X. Tian, J. X. Yan, W. Xiao, and W. T. Geng, Effect of lateral contraction and magnetism on the energy release upon fracture in metals: First-principles computational tensile test, *Phys. Rev. B* 79 (2009) 144114 (10pp).

- [39] A. R. Troiano, The role of hydrogen and other interstitials in the mechanical behavior of metals, *Trans. ASM* 52 (1960) 54–80.
- [40] Y. A. Du, J. Rogal, and R. Drautz, Diffusion of hydrogen within idealised grains of bcc-Fe: A kinetic Monte Carlo study, *Phys. Rev. B* 86 (2012) 174110 (13pp).
- [41] F. J. H. Ehlers, M. Seydou, D. Tingaud, F. Maurel, S. Queyreau, and Y. Charles, Ab initio studies of two Al grain boundaries subjected to mixed tension/shear mode loading: how shear may promote breakage, *Modelling Simul. Mater Sci. Eng.* 25 (2017) 064001 (17pp).
- [42] L. Ismer, M. S. Park, A. Janotti, and C. G. Van de Walle, Interactions between hydrogen impurities and vacancies in Mg and Al: A comparative analysis based on density functional theory, *Phys. Rev. B* 80 (2009) 184110 (10pp).
- [43] C. Quirós, J. Mougnot, G. Lombardi, M. Redolfi, O. Brinza, Y. Charles, A. Michau, and K. Hassouni, Blister formation and hydrogen retention in aluminium and beryllium: A modeling and experimental approach, *Nucl. Mater. Energ.* 12 (2017) 1178–1183.
- [44] L. Goodwin, R. J. Needs, and V. Heine, A pseudopotential total energy study of impurity promoted intergranular embrittlement, *J. Phys.: Condens. Matter* 2 (1990) 351–365.
- [45] A. M. Tahir, R. Janisch, and A. Hartmaier, Hydrogen embrittlement of a carbon segregated  $\Sigma 5(310)[001]$  symmetrical tilt grain boundary in  $\alpha$ -Fe, *Mater. Sci. Eng. A* 612 (2014) 462–467.
- [46] J. Song and W. A. Curtin, A nanoscale mechanism of hydrogen embrittlement in metals, *Acta Mater.* 59 (2011) 1557–1569.
- [47] K. Momma and F. Izumi, Vesta 3 for three-dimensional visualization of crystal, volumetric and morphology data, *J. Appl. Crystallogr.* 44 (2011) 1272–1276.